Supplementary Information:

Velocity Dependence of Moiré Friction

Yiming Song,[†,1] Xiang Gao,[†,2] Antoine Hinaut,[1] Sebastian Scherb,[1] Shuyu Huang,[1,3] Thilo Glatzel,[1] Oded Hod,[*,2] Michael Urbakh,[*,2] Ernst Meyer[*,1]

[1]Department of Physics, University of Basel, Basel 4056, Switzerland.

[2]Department of Physical Chemistry, School of Chemistry, The Raymond and Beverly Sackler Faculty of Exact Sciences and The Sackler Center for Computational Molecular and Materials Science, Tel Aviv University, Tel Aviv 6997801, Israel.

[3]Key Laboratory for Design and Manufacture of Micro-Nano Biomedical Instruments, School of Mechanical Engineering, Southeast University, Nanjing 211189, China.

*Corresponding authors: Email: urbakh@tauex.tau.ac.il, odedhod@tauex.tau.ac.il, ernst.meyer@unibas.ch

In this supplemental material, we provide additional details regarding the following aspects of the study reported in the main text:

1. Sample Preparation
2. Tip Preparation
3. Force Calibration
4. Molecular Dynamics Simulations
5. Detailed Derivation of the Phenomenological Model

1. Sample Preparation

The monolayer graphene film was grown in ultra-high vacuum (UHV, $\leq 1 \times 10^{-10}$ mbar) on a freshly prepared Pt(111) single-crystal surface. The Pt(111) surface was prepared by several cycles of Ar^+ ion sputtering ($1200 - 1800$ eV, chamber pressure 3×10^{-6} mbar for 10 min.) and annealing, using a home-made radio frequency (RF) heater (shown in Figure S1.). For the annealing process, the sample was heated to 1200 ℃ and kept at this temperature for 20 min. followed by a 5 min cooling period. Graphene was prepared by means of high-temperature flash in UHV. The sample was heated to 800 ℃ with the RF heater, while the precursor gas, ethylene (C_2H_4), was dosed onto the hot surface directly via a nozzle at a distance of 10– 20 mm. During the dosing process, the chamber pressure was maintained at a value of 2×10^{-8} mbar. After 2 min of dosing, the sample was maintained at a temperature of 800 ℃ for an extra 20 min., and then cooled down at a rate of 1 ℃/sec down to room temperature.

2. Tip Preparation

Prior to performing friction force measurements, the atomic force microscope (AFM) cantilever (PPP-CONT, Nanosensors) was annealed in UHV at a temperature of 200 ℃ for 2 h resulting in the removal of residual contaminants from the surface of the AFM tip. This was followed by Ar^+ ion sputtering of the tip for 2 min to remove the native silicon dioxide covering the tip.

3. Force Calibration

The normal spring constant k_N and lateral spring constant k_L of the rectangular cantilevers are given by:[1]

$$k_N = \frac{Ewt^3}{4L^3} \tag{S1}$$

$$k_L = \frac{Gwt^3}{3h^2L} \tag{S2}$$

where w is the width, L is the length, and t is the thickness of the cantilever, h is the height of the tip and E and G are the Young and shear moduli of the material. To evaluate the spring constants, the cantilever width and length can be determined via scanning electron microscopy, as shown in Figure S2. Furthermore, the resonance frequency, f_0, of the cantilever has been measured to obtain an accurate value of the cantilever thickness via the relation:[1]

$$t = \frac{2\sqrt{12}\pi}{1.875^2}\sqrt{\frac{\rho}{E}}f_0 L^2 \quad \text{(S3)}$$

where ρ is the density of the cantilever material.

Given the values of the spring constants, k_N and k_L, the force calibration proceeds with determining the photodetector sensitivity, S_z, which is evaluated by performing a standard force curve measurement, where the AFM tip is forced onto a hard surface until a certain deflection of the cantilever is reached and then it is retracted. During this process, the displacement of the AFM stage along the vertical (z) direction and the signal of photodiode detector are recorded. The slope of the linear part of the force curve gives S_z. Finally, the normal and lateral forces can be estimated via the relations:[2]

$$F_N = k_N \times S_Z \times V_N \quad \text{(S4)}$$

and

$$F_L = \frac{3}{2} \times k_L \times \frac{h}{L} \times S_Z \times V_L, \quad \text{(S5)}$$

where V_N, V_L are the respective voltages measured by the photodiode.

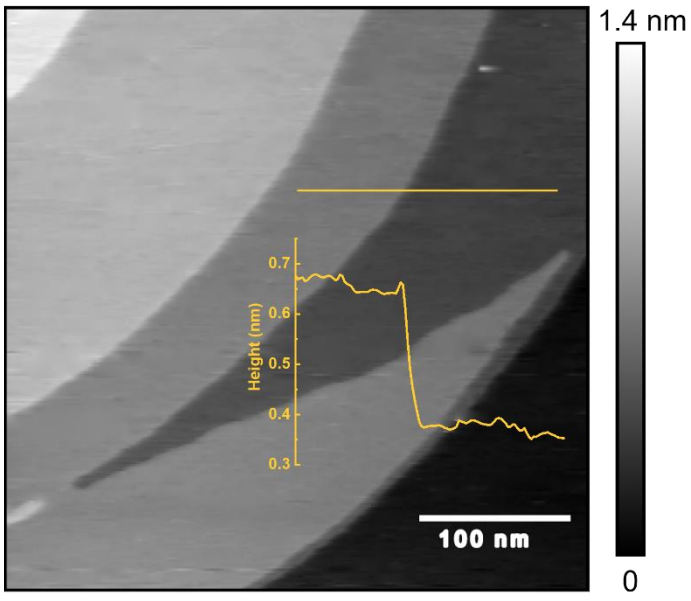

Figure S1: AFM image of an atomically clean Pt(111) surfaces prepared prior to graphene growth. The height profile across a single atom step edge (yellow curve) was measured using non-contact AFM.

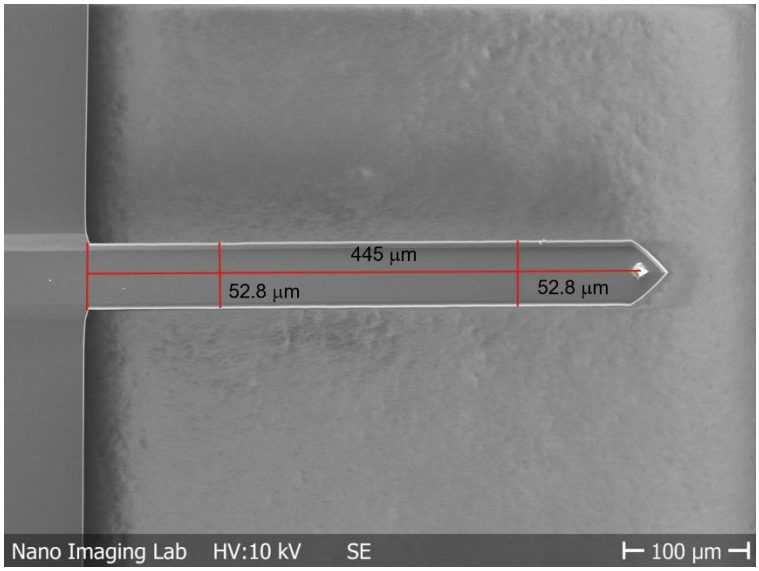

Figure S2: Scanning electron microscopy image of the AFM cantilever used to determine its length and width.

4. Molecular Dynamics Simulations

The molecular dynamics (MD) simulation model system consists of a 2.5-nm-radius hemispherical diamond tip sliding atop a graphene layer supported by a 1.36 nm thick Pt(111) substrate, as shown in Fig. S3a. The fact that the experimental tip is made of silicon, should have little effect on the qualitative nature of our simulation predictions. Since these are used to identify the main physical ingredients of the underlying frictional mechanisms that should be included in the phenomenological model, a correct qualitative description is sufficient. The specific experimental conditions (including the nature of the tip) are then accounted for by fitting the parameters of the phenomenological model to the experimental results.

The inter-atomic interactions within the diamond tip and the graphene layer are described with the second-generation reactive empirical bond order (REBO) potential.[3] The inter-atomic interactions within the Pt substrate are described via the embedded-atom-method (EAM) potential.[4] Because the main source of frictional dissipation in our setup is attributed to the interaction of the sliding tip with the moiré ridges, rather than the corrugated atomic potential, we can safely use the isotropic Lennard-Jones (LJ) potential to describe the cross interactions between the tip, graphene layer, and Pt substrate atoms. The LJ parameters for the diamond/graphene carbon atom interactions are taken to be $\sigma_{\mathrm{CC}} = 3.4$ Å and $\varepsilon_{\mathrm{CC}} = 0.00284$ eV.[5] For carbon and Pt we use $\sigma_{\mathrm{CPt}} = 2.936$ Å and $\varepsilon_{\mathrm{CPt}} = 0.04092$ eV,[6] for both the tip-substrate and the graphene-substrate interactions. The moiré

superstructures generated by this approach demonstrate similar corrugation as obtained in previous experiments.[7] All simulations are carried out using the LAMMPS package.[8]

To rationalize the experimental results, we generate three different moiré superstructure models with periods of 0.4, 1.0, and 2.2 nm by rotating the graphene surface counterclockwise with respect to the underlying Pt(111) substrate and annealing the graphene and Pt(111) substrate at 300 K. For the smaller superstructures studied, with moiré periods of 0.4 nm and 1.0 nm, finite graphene sheets of lateral dimensions of 20.7×16 nm^2 and 24.8×24.1 nm^2, respectively, are considered. For these model systems, minor rotation may occur during the annealing stage, with negligible effect on the calculated friction forces. For the larger superstructure studied, with a moiré period of 2.2 nm, a model system of lateral dimensions of 23.8×16.4 nm^2 is considered with periodic boundary conditions along the sliding direction and open boundary conditions along the perpendicular lateral direction. The moiré superstructures obtained using this procedure are presented in Fig. S4. The hemi-spherical diamond tip model consists of two rigid layers, located at the top of the tip, and all other tip atoms are unconstrained (see Fig. S3b). The diamond tip is placed on the annealed graphene layer with the center of mass of its rigid part located at one of the moiré pattern centers (away from any ridges). The geometry of the combined system is then further relaxed under an external normal load (the same load used in the corresponding dynamic simulation) using the FIRE algorithm[9, 10] with a convergence force criteria of 10^{-4} eV/Å. The normal load is applied by adding a vertical constant force on each of the atom in the rigid part of the tip, with magnitude ranging from 0 to 0.04 nN/atom, corresponding to an overall normal load in the range of 0 to 24.5 nN. To keep the lateral position of the rigid part of the tip at the moiré center during this minimization stage, the lateral forces acting on the rigid tip section are nullified.

The zero-temperature dynamic simulations are performed by driving the diamond tip with a dummy atom, mimicking a moving stage, via a spring with stiffness of 10 N/m coupled to the center of mass of the rigid part of the tip. The dummy atom moves with a constant velocity of $|\vec{v}_0| = 2$ m/s along the moiré lattice direction for each moiré configuration (see Fig. S4). To evacuate the heat generated at the shear interface, velocity damping with a damping coefficient of $\eta = 1.0$ ps^{-1} is applied to remote flexible regions of the tip and the Pt(111) far away from the sliding interface (see Figure S3b) To that end, we apply a damping force of $\mathbf{f}^i_{\mathrm{damp,tip}}(t)$ and $\mathbf{f}^i_{\mathrm{damp,Pt}}(t)$ to each atom, i, within the damped regions in the tip and Pt substrate, respectively, using the following equations:

$$\begin{cases} \mathbf{f}^i_{\mathrm{damp,tip}}(t) = -m_{\mathrm{C}}\eta\left(v^i_x(t) - v_{0,x}\right)\hat{\mathbf{x}} - m_{\mathrm{C}}\eta\left(v^i_y(t) - v_{0,y}\right)\hat{\mathbf{y}} - m_{\mathrm{C}}\eta v^i_z(t)\hat{\mathbf{z}} \\ \mathbf{f}^i_{\mathrm{damp,Pt}}(t) = -m_{\mathrm{Pt}}\sum_{\alpha=x,y,z}\eta v^i_\alpha(t)\,\hat{\boldsymbol{\alpha}} \end{cases}. \qquad \text{(S6)}$$

Here, m_{C} and m_{Pt} are the atomic masses of carbon and Pt, respectively, $v_{\alpha}^{i}(t)$ is the α Cartesian velocity component of the damped i^{th} atom at time t, $v_{0,x}$ and $v_{0,y}$ are the x and y components of sliding velocity $\vec{v}_0$, respectively, and $\hat{\boldsymbol{\alpha}} = \hat{\mathbf{x}}, \hat{\mathbf{y}}, \hat{\mathbf{z}}$ are the unit vectors along the Cartesian x, y and z directions, respectively. Note that lateral damping in the tip is applied according to the velocities relative to that of the moving stage, accounting for the fact that in realistic scenarios viscous dissipation is caused by the internal degrees of freedom of the sheared bodies. To prevent global sliding of the graphene layer due to the tip motion, the carbon atoms residing at the graphene layer edges nearly parallel to the sliding direction (see purple regions in Fig. S3) are constrained to their initial position via springs of stiffness 0.176 N/m. For each normal load and moiré configuration, the dynamic simulation last for 5 ns, with the first two nanoseconds discarded to avoid inclusion of transient effects in the analysis. The spring force exerted on the dummy atom is recorded, where resistive force is defined as positive and assistive force as negative. Figure S5 presents the smoothed lateral force traces presented in the Fig. 5 of the main text along with the corresponding raw data.

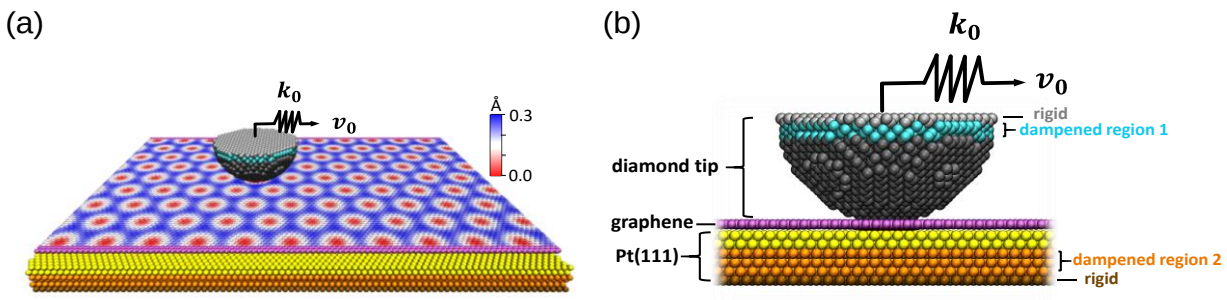

Figure S3: MD simulation setup. (a) Perspective view of the simulation model system with moiré superlattice dimension of ~2.2 nm. (b) Side view of the tip region presented in panel (a). Brown, orange, and yellow spheres in the substrate region represent rigid, dampened, and flexible Pt atoms. Light-gray, cyan, and dark-gray spheres in the tip region represent rigid, dampened, and flexible carbon atoms. The unconstrained graphene layer atoms are color coded according to their out-of-plane corrugation (see color bar in panel (a)), and the constrained graphene atoms are represented by purple spheres.

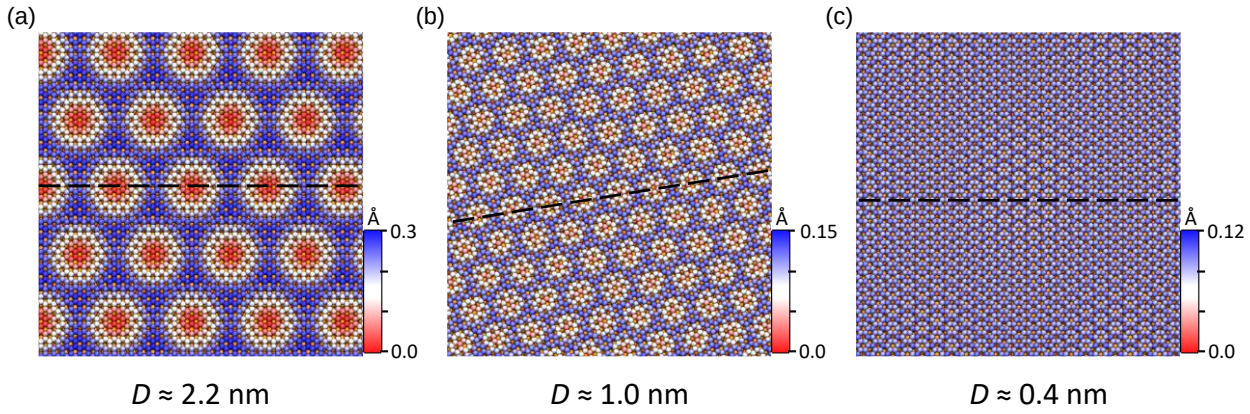

Figure S4: Out-of-plane deformation of three different moiré superstructures of periods: (a) 2.2 nm; (b) 1.0 nm; and (c) 0.4 nm. The color scales represent the out-of-plane corrugation of the graphene layer. The black dashed lines denote the moiré lattice directions chosen as the corresponding scan lines.

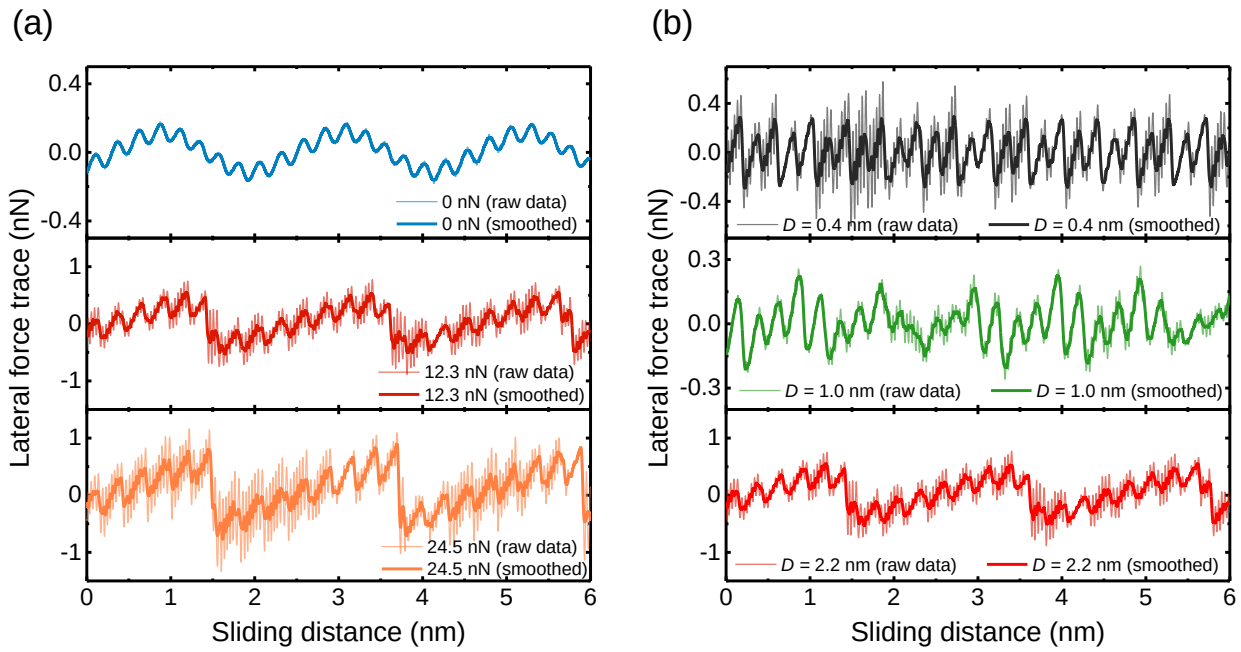

Figure S5: Raw (thin lines) versus smoothed (thick lines) lateral force traces. (a) Lateral force traces obtained for moiré superstructure dimension of 2.2 nm, under zero normal load (blue), and normal loads of 12.3 (red) and 24.5 nN (orange). (b) Lateral force traces obtained for moiré supercell dimensions of 0.4 (black), 1.0 (green), and 2.2 nm (red) under a normal load of 12.3 nN. In Fig. 5 of the main text we presented the smoothed lateral force traces.

5. Detailed Derivation of the Phenomenological Model

In this section, we provide a derivation of the analytical expression for the friction force obtained via the phenomenological model introduced in the main text. Within this model, a tip is pulled towards a moiré ridge through an elastic spring that connects it to a stage moving at constant velocity, v. The interactions between the tip and the moiré ridge and the pulling spring are described by potentials that are schematically shown in Fig. S6. The tip-stage interaction (dashed orange line) is given by a simple harmonic potential, where the force experienced by the tip is given by $F = \kappa(x_s - x_t)$ where κ is the effective spring constant, x_t is the tip position, and x_s is the stage position. The tip-ridge interactions (solid blue line) are described by a reactive potential. The minimum of this potential corresponds to the equilibrium tip-ridge distance between the tip and the ridge at the attached state. At infinite, the two are detached and do not interact. At intermediate distances, we introduce a small energy barrier for attachment (ΔE_a^0), which reflects the fact that both ridge and tip sections are of finite dimensions, hence when the tip approaches the ridge parts of it can be in the repulsive region, while other parts can be in the attractive region. The balance between the two can induce an energy barrier. Importantly, the barrier accounts for possible scenarios where the tip climbs atop the ridge instead of attaching to it - scenarios that cannot otherwise be captured by a one-dimensional model. The corresponding barrier for detachment, ΔE_d^0, is measured between the tip-ridge potential minimum the top of the barrier, which are separate by a distance of x_0.

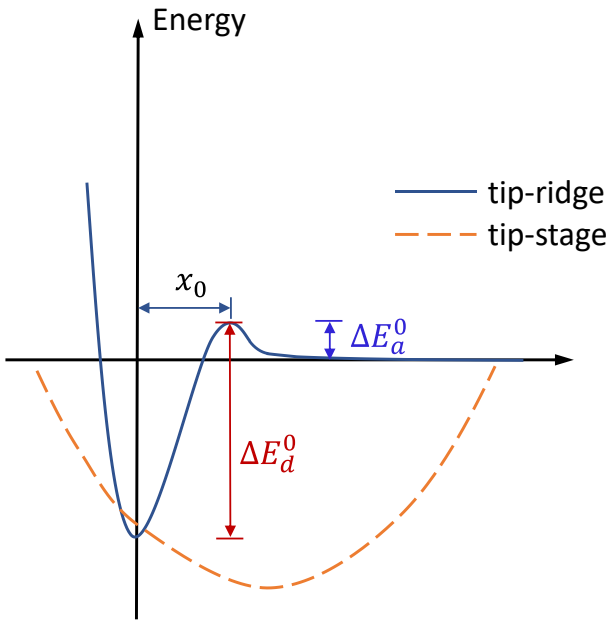

Figure S6: Schematic illustration of the one-dimensional tip-ridge (solid blue line) and tip-stage (dashed orange line) potentials used to construct the phenomenological model.

The total potential experienced by the tip is the sum of the two potentials. Hence, in the total potential the attachment and detachment barriers are varied due to the stage motion. For detachment the pulling spring will promote detachment hence effectively reducing the detachment barrier. This reduction can be evaluated from the elastic contribution of the spring when pulling the tip from its attached position ($x_t = 0$) to the top of the barrier ($x_t = x_0$):

$$\Delta E_d = \frac{1}{2}\kappa(x_s - x_0)^2 - \frac{1}{2}\kappa x_s^2 = -\kappa x_s x_0 + \frac{1}{2}\kappa x_0^2. \tag{S7}$$

For the attachment process, as long as the tip is free, it follows the position of the stage along the minimum of the harmonic potential, defined as 0. At the top of the barrier, the energy is the same as described above. Therefore, the effective increase in barrier height in the combined potential is given by:

$$\Delta E_a = \frac{1}{2}\kappa(x_s - x_0)^2 - 0 = \frac{1}{2}\kappa(x_s - x_0)^2. \tag{S8}$$

These spring induced changes of effective energy barrier heights ΔE_d and ΔE_a affect the detachment and attachment rates, which can be now written using the Arrhenius relation as:

$$\begin{cases} k_d = k_d^0 \exp(-\beta \Delta E_d) \\ k_a = k_a^0 \exp(-\beta \Delta E_a) \end{cases}, \tag{S9}$$

where $\beta = 1/k_\mathrm{B}T$, T is the temperature, k_B is the Boltzmann constant, and k_d^0 and k_a^0 are the detachment and attachment rates in the absence of interaction with the stage. Substituting Eqs. S7 and S8 into Eq. S9 then yields:

$$\begin{cases} k_d = k_d^0 \exp\left[\beta\kappa x_s x_0 - \frac{\beta\kappa}{2} x_0^2\right] \\ k_a = k_a^0 \exp\left[-\frac{\beta\kappa}{2}(x_s - x_0)^2\right] \end{cases}. \tag{S10}$$

To obtain Eq. (2) of the main text, which is originally derived to describe single-molecule force measurements,[11] we assume that the tip-spring potential is much softer than the tip-ridge potential. Hence, upon pulling the attached tip will stay at the minimum of the tip-ridge potential until the stage-tip spring is stretched to the point where detachment occurs. With this, the applied force is given by $F = \kappa(x_s - x_t) = \kappa x_s$. Substituting this into Eq. (S10) we arrive at Eq. (2) of the main text:

$$k_d(F) = k_d^0 \exp\left[\beta\left(F x_0 - \frac{1}{2}\kappa x_0^2\right)\right].$$

To obtain a similar expression for the detachment rate, we need to make one further assumption that during a detachment event, the position of the slider hardly changes, such that we can use the same expression for $x_s = F/\kappa$. This yields Eq. (3) of the main text:

$$k_a(F) = k_a^0 \exp\left[-\frac{\beta\kappa}{2}(F/\kappa - x_0)^2\right].$$

In order to derive Eq. (6) for the friction force presented in the main text, it should be taken into account that when the tip is attached to the ridge, following any detachment process at a pulling force smaller than F_{eq} (the force at which the detachment and attachment rates are equal, $k_d(F) = k_a(F)$) it will quickly snap back to the attached state. Therefore, for $F < F_{eq}$, the tip will be mainly trapped in the attached state, so that the measured detachment force cannot be smaller than F_{eq}.[11] For forces higher than F_{eq}, the attachment barrier rapidly increases and the attachment rate reduces accordingly. This allows us to neglect the second term on the right-hand side of the master equation (1) of the main text for $F > F_{eq}$:

$$\frac{dp_a(t)}{dt} \cong -k_d(t)p_a \tag{S11}$$

Recalling that the stage is moving at constant velocity $x_s = vt$, and assuming that at $t = 0$ the tip is at the attached state $x_t = 0$ we may write:

$$F = \kappa(x_s - x_t) = \kappa x_s = \kappa v t$$

Using this relation in Eq. (S11) and rearranging the terms we find that:

$$\int_1^{p_a} \frac{dp_a}{p_a} \cong -\frac{1}{\kappa v}\int_{F_{eq}}^{F} k_d(f)df = -\frac{1}{\kappa v}\int_{F_{eq}}^{F} k_d^0 \mathrm{e}^{\beta\left(Fx_0 - \frac{1}{2}\kappa x_0^2\right)}df. \tag{S12}$$

Eq. (S12) can be solved as:

$$p_a(F) = \exp\left\{\frac{F_\beta}{\kappa v}\left[k_d\left(F_{eq}\right) - k_d(F)\right]\right\}, \tag{S13}$$

where $F_\beta = k_\mathrm{B}T/x_0$ .Then, the mean detachment force $\langle F_d \rangle$ can be calculated by averaging the force F with the detachment probability density, calculated as the reduction in the probability to be at the attached state with increasing pulling force, $-\frac{dp_a(F)}{dF}$:

$$\langle F_d \rangle = \int_{F_{eq}}^{\infty}\left(-\frac{dp_a(f)}{df}\right)f df. \tag{S14}$$

Performing integration by parts in Eq. (S14) we obtain:

$$\langle F_d \rangle = \int_{F_{eq}}^{\infty} \left[-\frac{d(p_a(f)f)}{df} + p_a(f) \right] df = -p_a(f)f \Big|_{F_{eq}}^{\infty} + \int_{F_{eq}}^{\infty} p_a(f) df =$$

$$= F_{eq} + \exp\left(\frac{F_\beta k_d(F_{eq})}{\kappa v}\right) \int_{F_{eq}}^{\infty} \exp\left(-\frac{F_\beta k_d(f)}{\kappa v}\right) df \overset{s \equiv \frac{F_\beta k_d(f)}{\kappa v}}{=}$$

$$= F_{eq} + \exp\left(\frac{F_\beta k_d(F_{eq})}{\kappa v}\right) \int_{\frac{F_\beta k_d(F_{eq})}{\kappa v}}^{\infty} \frac{F_\beta}{s} \exp(-s) ds = F_{eq} + F_\beta \exp\left(\frac{F_\beta k_d(F_{eq})}{\kappa v}\right) E_1\left(\frac{F_\beta k_d(F_{eq})}{\kappa v}\right)$$

$$= F_{eq} + F_\beta \exp\left(\frac{v^*}{v}\right) E_1\left(\frac{v^*}{v}\right), \tag{S15}$$

where $v^* = F_\beta k_d(F_{eq})/\kappa$, and we have used the relation

$$\frac{ds}{dF} = \frac{F_\beta}{\kappa v} \frac{dk_d(F)}{dF} = \frac{F_\beta}{\kappa v} \frac{d}{dF} \left\{ k_d^0 \exp\left[\beta \left(F x_0 - \frac{1}{2} \kappa x_0^2 \right) \right] \right\} = \frac{1}{\kappa v \beta x_0} \beta x_0 k_d(F) = \frac{k_d(F)}{\kappa v} = \frac{s}{F_\beta}$$

or

$$\frac{dF}{ds} = \frac{F_\beta}{s}.$$

Considering that in the overdamped stick-slip regime of motion, described by the two-state model, the lateral force increases linearly in time when the tip is in the trapped state and then drops to zero after the detachment, the time-averaged friction force, $\langle F \rangle$ can be calculated from the corresponding triangular area under the force trace of a single stick-slip event (see schematic illustration of Fig. S7) as $1/2\langle F_d \rangle$, yielding Eq. (6) of the main text.

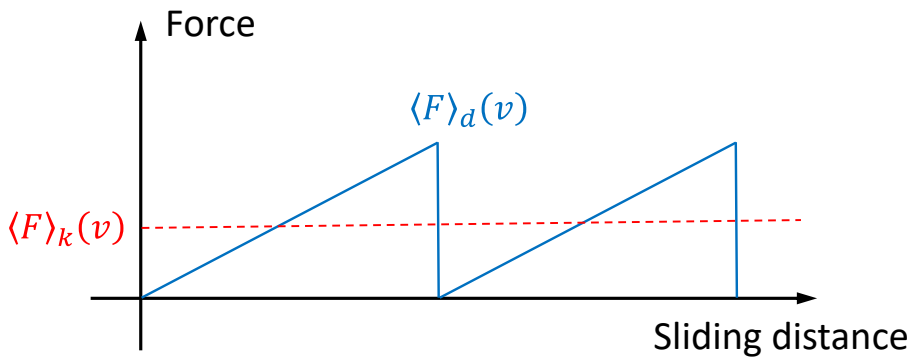

Figure S7: Schematic illustration of the relation between detachment force $\langle F \rangle_d(v)$ and the kinetic friction $\langle F \rangle_k(v)$ assumed in the model.

References:

1. Meyer, E.; Hug, H. J.; Bennewitz, R., Force Microscopy. In *Scanning Probe Microscopy: The Lab on a Tip*, Meyer, E.; Hug, H. J.; Bennewitz, R., Eds. Springer Berlin Heidelberg: Berlin, Heidelberg, 2004; pp 45-95.
2. Meyer, E.; Gyalog, T.; Overney, R. M.; Dransfeld, K., *Nanoscience: Friction And Rheology On The Nanometer Scale*. World Scientific: 1998.
3. Brenner, D. W.; Shenderova, O. A.; Harrison, J. A.; Stuart, S. J.; Ni, B.; Sinnott, S. B. A second-generation reactive empirical bond order (REBO) potential energy expression for hydrocarbons. *J. Phys.: Condens. Matter* **2002,** 14, 783-802.
4. Foiles, S. M.; Baskes, M. I.; Daw, M. S. Embedded-atom-method functions for the fcc metals Cu, Ag, Au, Ni, Pd, Pt, and their alloys. *Phys. Rev. B* **1986,** 33, 7983-7991.
5. Stuart, S. J.; Tutein, A. B.; Harrison, J. A. A reactive potential for hydrocarbons with intermolecular interactions. *J. Chem. Phys.* **2000,** 112, 6472-6486.
6. Sun, B.; Ouyang, W.; Gu, J.; Wang, C.; Wang, J.; Mi, L. Formation of Moiré superstructure of epitaxial graphene on Pt(111): A molecular dynamic simulation investigation. *Mater. Chem. Phys.* **2020,** 253, 123126.
7. Gao, M.; Pan, Y.; Huang, L.; Hu, H.; Zhang, L. Z.; Guo, H. M.; Du, S. X.; Gao, H. J. Epitaxial growth and structural property of graphene on Pt(111). *Appl. Phys. Lett.* **2011,** 98, 033101.
8. Plimpton, S. Fast Parallel Algorithms for Short-Range Molecular Dynamics. *J. Comput. Phys.* **1995,** 117, 1-19.
9. Bitzek, E.; Koskinen, P.; Gähler, F.; Moseler, M.; Gumbsch, P. Structural Relaxation Made Simple. *Phys. Rev. Lett.* **2006,** 97, 170201.
10. Guénolé, J.; Nöhring, W. G.; Vaid, A.; Houllé, F.; Xie, Z.; Prakash, A.; Bitzek, E. Assessment and optimization of the fast inertial relaxation engine (fire) for energy minimization in atomistic simulations and its implementation in lammps. *Comput. Mater. Sci.* **2020,** 175, 109584.
11. Friddle Raymond, W.; Noy, A.; De Yoreo James, J. Interpreting the widespread nonlinear force spectra of intermolecular bonds. *Proc. Natl. Acad. Sci. U.S.A.* **2012,** 109, 13573-13578.